Materials Horizons

ROYAL SOCIETY OF CHEMISTRY

COMMUNICATION

View Article Online
View Journal

Cite this: DOI: 10.1039/d6mh00177g

Received 29th January 2026,
Accepted 28th April 2026

DOI: 10.1039/d6mh00177g

rsc.li/materials-horizons

Printable, self-healing and recyclable PEDOT:PSS/polyurethane composites for durable bioelectronics

Jinsil Kim and Fabio Cicoira *

The development of self-healing conductors that are simultaneously printable, recyclable, and resilient to severe mechanical damage remains a key challenge for flexible bioelectronic technologies. Here, we report a multifunctional composite based on poly(3,4-ethylenedioxythiophene):polystyrene sulfonate (PEDOT:PSS) blended with a custom-designed polyurethane (PU) incorporating dynamic disulfide bonds and hydrogen-bonding motifs. This materials design enables autonomous room-temperature healing from scratches, cuts, and punctures, without external stimuli, while preserving mechanical integrity and electrical continuity. The composite is processable from green solvents and can be spin-coated or printed into uniform, transparent, and highly stretchable films, as well as free-standing membranes transferable to diverse substrates. Optimized PEDOT:PSS/PU/Gly films exhibit a functional conductivity (~15 S cm^{-1}), high stretchability (>650%), strong self-adhesion, and stable performance under repeated deformation. Importantly, the material supports both mechanical reuse and chemical recycling over at least 15 cycles, retaining more than 90% of its mechanical strength and fully recovering its electrical conductivity. Mechanistic investigations reveal that reversible disulfide exchange and hydrogen bond reformation govern rapid network reorganization and efficient self-repair. Printed electronic tattoos and free-standing electrodes fabricated from this composite deliver low-impedance and high-fidelity electrocardiogram (ECG) recordings. Together, these results establish a sustainable and versatile materials platform that advances self-healing conductors beyond superficial damage, providing a practical pathway toward durable and recyclable bioelectronic materials and devices.

New concepts

This work demonstrates a damage-tolerant and circular materials concept for soft and flexible electronics, realized through a printable conducting polymer composite that autonomously heals at room temperature from realistic mechanical failures, including scratches, cuts, and solid-state puncture damage. Unlike most self-healing conductors that focus on minor surface damage or require gels, encapsulated liquids, or external stimuli, this platform operates in fully solid, micrometre-thick films compatible with scalable fabrication. The key differentiation lies in the simultaneous integration of autonomous self-healing, strong self-adhesion, printability, and dual recycling pathways (mechanical remoulding and chemical component recovery) within a single conducting material system—capabilities that are rarely achieved together. Beyond performance metrics, this work provides insight into how dynamic covalent and reversible non-covalent interactions can be balanced to enable damage resilience without compromising processability or device relevance. By demonstrating both single-use electronic tattoos and reusable freestanding electrodes with stable electrical performance, the underlying concept reframes self-healing conductors as reliable, repairable, and recyclable building blocks for next-generation flexible and bioelectronic technologies.

1. Introduction

Self-healing electronic materials are central to the development of flexible, wearable, and biointegrated devices because they can autonomously restore electrical and mechanical function after damage, thereby extending device lifetime and reducing electronic waste.[1,2] In wearable health monitoring, soft robotics, energy storage, and implantable bioelectronics, devices frequently undergo mechanical deformation, accidental damage, and repeated stress, making rapid and reliable self-repair essential.[3,4] Despite major progress, achieving the simultaneous combination of high conductivity, mechanical compliance, autonomous room-temperature (RT) healing, and recyclability in a single material platform remains a significant challenge.[5–7]

Most reported self-healing conductors are based on polymer composites or hydrogels that can restore electrical conductivity after scratches or cuts.[8,9] However, these systems are often processed by drop-casting, which produces thick and non-uniform films that limit integration into advanced architectures and impede scalable microfabrication.[10] Only a small number of self-healing conductors can be spin-coated or printed, even though thin-film processability is crucial for

Department of Chemical Engineering, Polytechnique Montréal, Montréal, QC H3C 3A7, Canada. E-mail: fabio.cicoira@polymtl.ca

optical transparency, pattern fidelity, and compatibility with established device manufacturing workflows.[11] Furthermore, free-standing transferable films, highly valuable for wearable electrodes and soft interfaces, are seldom available.[11,12]

Another limitation is the frequent need for external stimuli such as heat, pressure, or chemical agents to trigger repair.[13] For practical wearable and implantable applications, autonomous healing in ambient conditions is essential, as it allows immediate functional recovery without user intervention or energy input, reduces overall power consumption, and ensures compatibility with biological environments.[14] Moreover, while scratch and cut healing are well documented, puncture healing, one of the most severe and realistic mechanical failure modes, has received very limited attention.[15] Addressing puncture damage in a fully solid-state conductor is particularly important for flexible electronic systems, which are frequently exposed to accidental impact, handling-induced defects, and localized mechanical abuse during daily operation.

Poly(3,4-ethylenedioxythiophene) doped with polystyrene sulfonate (PEDOT:PSS) is among the most versatile and widely used conducting polymers, valued for its high conductivity, mechanical flexibility, aqueous processability, and intrinsic self-repair under humid conditions.[16,17] Its mechanical compliance is often enhanced through blending with flexible or functional additives such as poly(ethylene glycol) (PEG),[18] polyurethane diol (PUD),[19] tannic acid (TA),[20] Triton X-100,[21] and poly(vinyl alcohol) (PVA),[22] which can improve stretchability and enable self-healing. However, no PEDOT:PSS-based system has simultaneously offered thin-film printability or spin-coating, autonomous RT self-healing, including puncture recovery, and recyclability within the same material framework.

Recyclability remains an especially underexplored dimension in flexible electronics. Most self-healing conductors are challenging to reprocess, and their disposal contributes to the growing concern of electronic waste. Achieving chemical or mechanical recycling without compromising performance would significantly enhance the sustainability of these materials.[23] Polyurethanes (PUs) are attractive in this respect because their segmented architecture and dynamic covalent or supramolecular motifs can provide tunable mechanics, reversible bond exchange, and reprocessability. Its chemistry is highly tunable through the choice of polyols, which provide elasticity, diisocyanates and chain extenders, which control strength and flexibility.[24] Incorporating long polyol chains can further lower the glass transition temperature (T_g), improving chain mobility, healing dynamics, and solubility in green solvents, thereby facilitating both recyclability and solution processing spin-coating or printing.[25,26]

In this work, we address these unmet requirements by designing a polyurethane incorporating dynamic disulfide bonds and hydrogen-bonding soft segments and blending it with PEDOT:PSS to obtain a multifunctional, processable, and recyclable conductive composite. The resulting films can be spin-coated or printed into uniform, transparent thin and free-standing membranes, enabling precise thickness control and straightforward patterning. The composites combine high electrical conductivity ($\sim$15 S cm^{-1}), high stretchability ($>$650%), strong self-adhesion, and rapid room-temperature healing from scratches, cuts, and punctures. The films can also be recycled through both chemical and mechanical routes over multiple cycles with minimal performance loss, advancing the concept of circular flexible electronics. Beyond demonstrating multifunctional performance, we provide molecular-level insight into the autonomous healing process through solid-state FTIR analysis, revealing that reversible disulfide exchange and hydrogen-bond reformation govern damage recovery. Printed electronic-tattoo electrodes fabricated from this composite exhibit stable, low-impedance ECG recordings and enable facile water-assisted detachment and reuse. Rather than maximizing a single performance metric, this work demonstrates how printability, autonomous room-temperature self-healing, including solid-state puncture recovery, and true recyclability can be integrated within a single conducting polymer platform suitable for soft bioelectronics. Together, these results establish a unified PEDOT:PSS-based materials platform that integrates thin-film processability, robust room-temperature self-healing, and dual recyclability, addressing long-standing challenges in the development of durable, sustainable, and manufacturable soft electronic systems. By prioritizing damage tolerance, autonomous recovery, and recyclability in thin, printable films, this work directly targets reliability challenges central to flexible and wearable electronic technologies.

2. Results and discussion

2.1. Synthesis of polyurethane (PU)

A self-healing, stretchable, and recyclable polyurethane (PU) was synthesized using poly(ε-caprolactone) diol (PCL diol) and polyethylene glycol (PEG) as soft segments, to enhance chain mobility and solubility, together with isophorone diisocyanate (IPDI) as the hard segment to provide mechanical strength, aminophenyl disulfide (APDS) as the chain extender to introduce dynamic disulfide bonds, and trimethylolpropane (TMP) as the crosslinker (Fig. 1a). In our previous work, we reported a PU composed of PCL diol, IPDI, and 1,3-propanediol (PDO) which, when blended with PEG and PEDOT, exhibited self-healing and mechanical reprocessability at moderate temperatures ($\sim$50 °C), owing to the flexibility provided by the PCL segments.[24] To enable autonomous healing and reprocessing at room-temperature while improving solution-based processability, we designed a new PU incorporating PEG and disulfide bonds. PEG lowers the glass transition temperature (T_g) of the polymer network and enhances chain mobility, whereas disulfide bonds, widely exploited to improve the durability and sustainability of polymeric systems,[27,28] enable reversible bond exchange above T_g, promoting autonomous healing and reprocessability.

The PU synthesis followed a two-step polymerization. In the first step, hydroxyl terminated PCL diol and PEG reacted with the isocyanate groups of IPDI to form an –NCO-terminated prepolymer. In the second step, APDS and TMP were added to

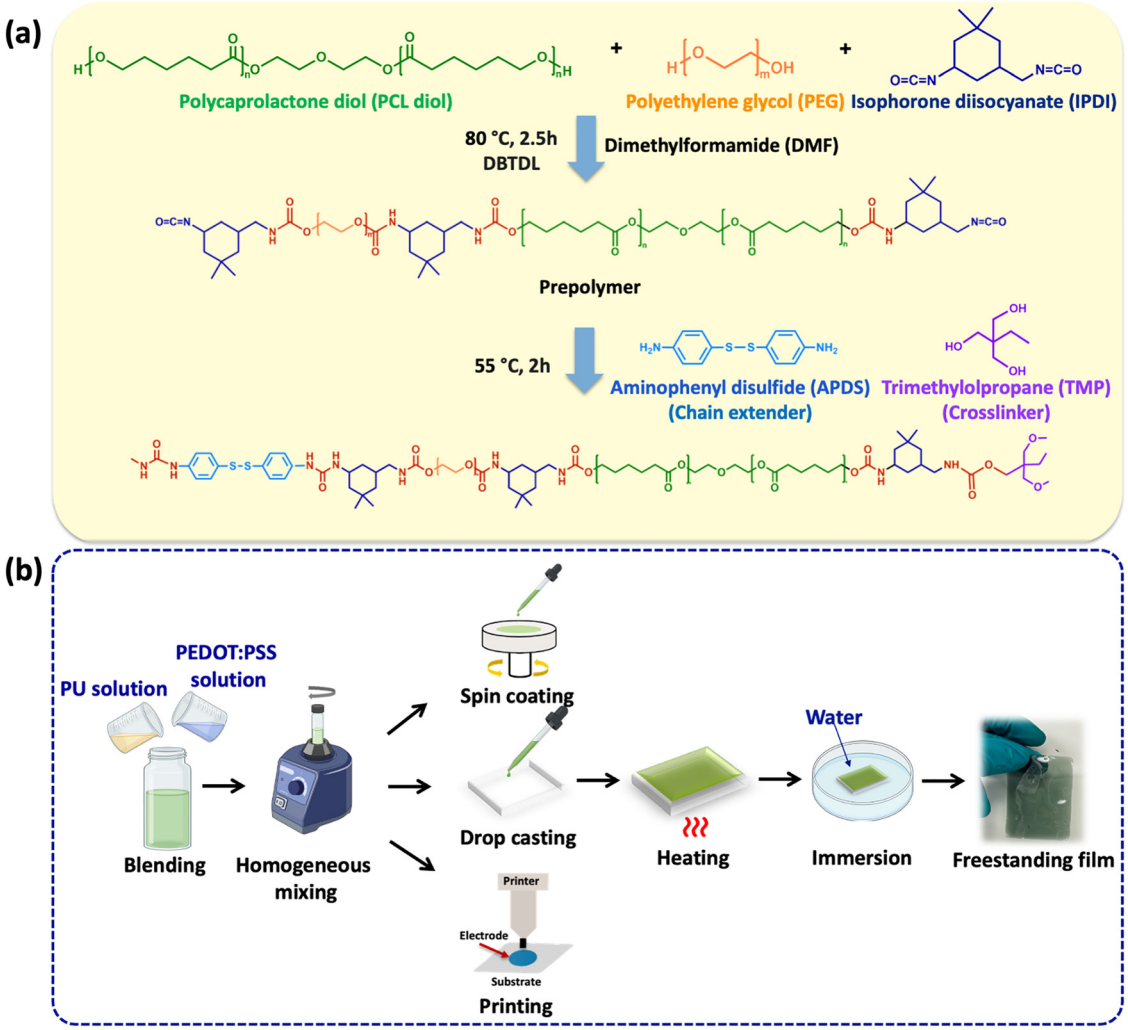

Fig. 1 (a) Schematic illustration of the synthetic route used to prepare the self-healing, stretchable, and recyclable polyurethane (PU). (b) Step-by-step fabrication of PEDOT:PSS/PU composites, including solution mixing, spin-coating, printing, and drop-casting onto glass substrates, followed by thermal curing and water-assisted release to obtain freestanding films.

extend the polymer chains and introduce both disulfide bonds and crosslinks. The characteristic absorption at 2270 cm^{-1} in the FTIR spectra (Fig. S1) of the prepolymer confirmed –NCO terminations, while its disappearance in the final PU indicated complete reaction of isocyanate groups. The appearance of the C═O (1700 cm^{-1}) and N–H (3200 cm^{-1}) stretching bands confirmed urethane bond formation. Mechanical characterization showed that the resulting PU was highly stretchable and robust, capable of withstanding twisting and knotting without mechanical failure (Fig. S2).

2.2. Formulation and processing versatility of conductive composites

Stretchable, self-healing, and recyclable conductive composites were obtained by drop casting blends the synthesized PU with PEDOT:PSS (Fig. 1b). As expected, the electrical conductivity decreased with increasing PU content compared to pure PEDOT:PSS printing paste (~50 S cm^{-1}): varying the PU concentration from 3.5 wt% to 18 wt% yielded conductivities ranging from ~20 S cm^{-1} to ~0.1 S cm^{-1} (Table 1). The addition of glycerol, known to promote PEDOT chain alignment and enhance conductivity,[35] raised the conductivity of high-PU-content composites to ~15 cm^{-1}.

A key advantage of the polyurethane developed in this study is its enhanced processing versatility. Incorporation of PEG segments lowers the glass transition temperature and increases solubility in polar green solvents, such as ethanol and anisole (Table S1), enabling the fabrication of uniform conducting films by drop-casting, spin-coating, and printing. This behavior represents a clear improvement over our previously reported polyurethane systems and many other self-healing materials (Table S3) and directly supports scalable manufacturing and integration into soft electronic devices.

Owing to this solvent compatibility, printable ethanol-based inks can be readily formulated, allowing high-fidelity patterning of stretchable and self-healing conducting films. When printed on glass substrates, the resulting features can be released by simple immersion in water and transferred onto

Table 1 Electrical conductivity, elongation at break, Young's modulus (measured in the 0–10% strain range), and adhesion of PEDOT:PSS/PU-based drop-cast films with varying compositions. Data are reported as the mean ± standard deviation, with each sample measured three times (n = 3)

Samples	PEDOT:PSS solution (wt%)	PU solution (wt%)	Glycerol (wt%)	Conductivity (S cm^{-1})	Elongation at break (%)	Young's modulus (MPa)	Adhesion	
							Glass	Itself
PEDOT:PSS/PU-3.5	96.5	3.5		22 ± 2				
PEDOT:PSS/PU-6	94.0	6.0		20 ± 2				
PEDOT:PSS/PU-10	90.0	10.0		2.4 ± 0.1				
PEDOT:PSS/PU-13	87.0	13.0		0.50 ± 0.02	202 ± 10	0.14 ± 0.04	0.16 ± 0.05	0.48 ± 0.16
PEDOT:PSS/PU-15	85.0	15.0		0.10 ± 0.03	432 ± 12	0.13 ± 0.02	0.31 ± 0.10	1.02 ± 0.37
PEDOT:PSS/PU-18	82.0	18.0		0.10 ± 0.01	500 ± 15	0.09 ± 0.03	0.59 ± 0.12	1.71 ± 0.42
PEDOT:PSS/PU-15/Gly-2.4	83.0	14.6	2.4	15 ± 2	545 ± 12	0.040 ± 0.01	0.97 ± 0.14	2.25 ± 0.50
PEDOT:PSS/PU-18/Gly-2.2	80.3	17.5	2.2	13 ± 2	630 ± 19	0.020 ± 0.002	1.35 ± 0.33	2.85 ± 0.71

other substrates or directly onto skin, providing a straightforward route to conformal, low-cost wearable electronic devices.

2.3. Mechanical and electromechanical properties

The mechanical and electromechanical properties of the drop-cast composites were examined to evaluate their stretchability, durability, and suitability for flexible electronic applications such as e-tattoos and freestanding electrodes. The corresponding mechanical parameters, including elongation at break, Young's modulus, and adhesion strength, are summarized in Table 1, revealing a clear correlation between PU/glycerol content and mechanical compliance.

2.3.1. Tensile properties. Stress–strain measurements (Fig. 2a and Fig. S3) revealed that increasing the PU content reduced the Young's modulus while simultaneously increasing the elongation at break, demonstrating enhanced flexibility and stretchability (Table 1). A lower modulus minimizes mechanical mismatch with human skin (0.01–0.1 MPa), whereas a higher elongation at break enables the films to accommodate large deformations without rupture.[20,29,30] Compared to our previous system, the stress–strain curves exhibited smooth profiles without a distinct yield point, consistent with the presence of dynamic disulfide bonds that facilitate chain rearrangement and energy dissipation through reversible bond exchange.[31,32] Incorporation of glycerol further improved the mechanical properties, leading to a pronounced decrease in modulus and a substantial increase in stretchability.[33,34] This improvement is attributed to glycerol's plasticizing action, which enhances chain mobility and strengthens interfacial interactions between PEDOT:PSS and PU.[35] Among the tested compositions, PEDOT:PSS/PU-18/Gly-2.2 exhibited the most balanced mechanical performance, combining an elongation at break of 630% with a low Young's modulus of 0.02 MPa. This elongation at break is comparable to values reported for highly stretchable conductive polymer systems and represents an approximately 1.5-fold improvement over our previously reported material (Table S2).

2.3.2. Cyclic durability. Cyclic loading–unloading tests (at 0–50% strain, 500 cycles) were conducted to simulate skin deformation and assess long-term mechanical durability. Representative curves for 500 cycles (Fig. S4a and b) show a large energy input during loading and pronounced energy dissipation, as indicated by the hysteresis between loading and unloading curves, with the largest hysteresis observed in the first cycle. With repeated cycling, energy recovery progressively increased and stabilized (Fig. S5), indicating gradual rearrangement of the dynamic network into a stable configuration. Among all formulations, PEDOT:PSS/PU-18/Gly-2.2 exhibited the highest energy recovery (~75%), with energy dissipation decreasing from 145 to 110 kJ m^{-3} and stabilizing after 100 cycles. The material retained its mechanical integrity after 500 cycles, confirming excellent fatigue resistance. This stabilization behavior, typical of networks containing dynamic covalent bonds, reflects gradual chain rearrangement and network reorganization into a stable configuration under repeated stress.

2.3.3. Electromechanical stability. The relative resistance (R/R_0) was measured under a constant bias of 0.2 V during

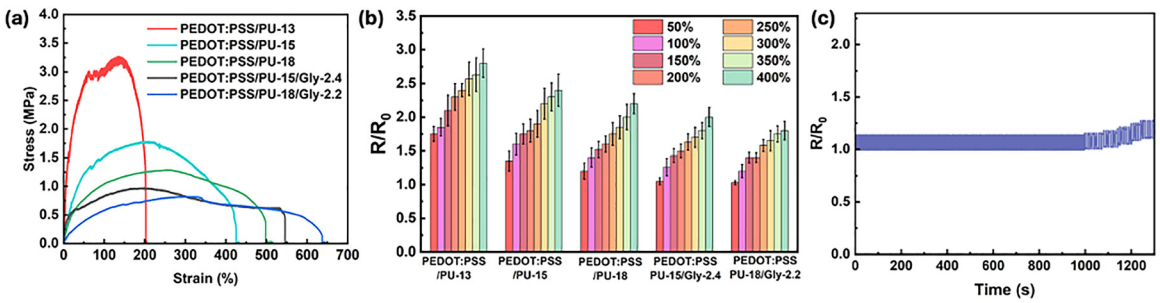

Fig. 2 (a) Tensile stress–strain curves of PEDOT:PSS/PU-based films. (b) Relative resistance (R/R_0) measured under a constant 0.2 V bias during uniaxial stretching to 50%, 100%, 150%, 200%, 250%, 300%, 350%, and 400% strain at a rate of 10 mm min^{-1}. Data are reported as the mean ± standard deviation (n = 3). (c) Resistance change (R/R_0) of a PEDOT:PSS/PU-18/Gly-2.2 film during 500 cyclic strain cycles between 0 and 50%. The inset shows a magnified view from 500 to 530 s, highlighting resistance variation during cyclic loading.

uniaxial stretching from 50% to 400% strain (Fig. S6). PEDOT:PSS/PU-18/Gly-2.2 consistently showed the smallest resistance variation (Fig. 2b), confirming superior electromechanical stability. Under cyclic deformation at 50% strain, R/R_0 fluctuations remained within ~10% over 500 cycles (Fig. 2c), significantly lower than other compositions (Fig. S7), which showed larger fluctuations and less stable responses. In addition, only a slight increase in the average R/R_0 of ~3–5% was observed up to 700 cycles, indicating stable conductive pathways under repeated mechanical stress. These results highlight the excellent mechanical–electrical coupling and fatigue resistance of the composite.

2.3.4. Adhesion performance. Adhesion tests confirmed strong self-adhesion, a key property for conformal skin contact (Fig. S8). PEDOT:PSS/PU-18/Gly-2.2 showed the highest adhesion strength, reaching 1.35 N cm^{-1} on glass (Fig. S8a) and 2.85 N cm^{-1} in self-adhesion tests (Table 1 and Fig. S8b). High PU content and glycerol likely promote reversible disulfide-mediated bond exchange at the interface.[36] In contrast, adhesion to glass relies primarily on weaker physical interactions, resulting in lower values.

Collectively, these findings position PEDOT:PSS/PU-18/Gly-2.2 as a versatile and durable materials platform that combines high stretchability, mechanical robustness, electromechanical stability, self-adhesion, and a functional conductivity (13 ± 2 S cm^{-1}), key attributes for next-generation e-tattoos and wearable bioelectronics designed to operate reliably under continuous mechanical deformation. Among all investigated compositions, this formulation consistently exhibited the most balanced performance across mechanical, electrical and adhesion properties. Therefore, PEDOT:PSS/PU-18/Gly-2.2 was selected as the primary research target for subsequent investigations. Furthermore, complementary experiments indicated that a minimum PU content of 15 wt% was required to achieve room-temperature self-healing; therefore, subsequent analyses focused on this formulation.

Cyclic voltammetry (CV) was used to assess the electrochemical response of the composite (Fig. S9). The curves show slightly non-ideal capacitive behavior with mild hysteresis between forward and reverse scans, which may be related to ion transport limitations and interfacial effects within the PEDOT:PSS/PU network. At higher voltages, an increase in current is observed, suggesting the possible onset of faradaic processes. Within the low-voltage range (<1 V) relevant for wearable bioelectronic applications, stable responses are maintained.

2.4. Electrical and mechanical self-healing

The dynamic disulfide chemistry that imparts strong adhesion and cyclic durability to the composites also governs their self-healing capability. These reversible interactions within the PU matrix enable rapid network reformation after mechanical damage, thereby restoring both mechanical integrity and electrical conductivity. Based on the overall performance, PEDOT:PSS/PU-18/Gly-2.2 was selected as a representative system to investigate self-healing behavior. Building on the excellent mechanical and electromechanical performance of the optimized composite, we investigated its ability to autonomously recover mechanical integrity and electrical conductivity after damage, a critical requirement for long-term reliability of wearable and stretchable electronic devices.

2.4.1. Electrical self-healing. Electrical and mechanical self-healing experiments were performed at 25 °C, a temperature slightly above the composite's glass transition temperature (T_g = 21 °C, Fig. S10a), providing sufficient chain mobility to enable the re-formation of reversible hydrogen bonds and disulfide bonds. All drop-cast PEDOT:PSS/PU films fully recovered their electrical conductivity after being cut with a razor blade (Fig. S11). Among them, PEDOT:PSS/PU-18/Gly-2.2 exhibited particularly rapid recovery, restoring conductivity within ~0.1 s with a healing efficiency of 99.7 ± 0.3%. Notably, this high efficiency was preserved in transparent spin-coated films as thin as 1.4–2.5 μm (Fig. 3a), a thickness regime in which complete electrical reconnection is often difficult to achieve. This behavior is attributed to the formation of highly uniform films by spin coating, whereas many previously reported self-healing conductors (Table S3) are primarily demonstrated using thicker, drop-cast films, for which electrical reconnection is less demanding. Across all investigated thicknesses, films recovered their conductivity within ~0.3 s and maintained healing efficiencies close to 100% over repeated cut–heal cycles. The minimum film thickness enabling full electrical recovery was determined to be 1.4 μm.

Spin-coated films deposited on glass and PET substrates exhibited high optical transmittance (~95.2 ± 0.7%, Fig. S12a and b), supporting their suitability for self-healing electrochromic and optoelectronic devices. This fabrication method also enables precise control over film thickness and uniformity, which is critical for optimizing transparency and overall device performance.

To further evaluate the self-healing performance under more demanding, device-relevant conditions, electrical self-healing was investigated using printed conductive lines (Fig. 3b). Each cut induced a sharp decrease in current, followed by rapid recovery upon healing (~0.5 s, 96.7 ± 0.5%). The current consistently returned close to its initial value after each damage event, demonstrating reproducible electrical self-healing behavior.

2.4.2. Mechanical self-healing. Mechanical self-healing was evaluated using cut–stick, scratch, and puncture tests. PEDOT:PSS/PU-18/Gly-2.2 exhibited near-complete recovery of elongation at break (98.0 ± 0.2%) following cut–stick healing. In contrast, PEDOT:PSS/PU-13, which contains the lowest PU fraction, showed a reduced recovery efficiency of 75.0 ± 2.2%. Increasing the PU content to 15% and 18% led to a corresponding improvement in healing efficiency. Notably, higher PU contents consistently preserved strong self-adhesive behavior, which correlates with the enhanced mechanical recovery (Fig. S13 and Movie S1). In scratch-healing experiments, surface damage was fully repaired within 1 h at 25 °C, as confirmed by optical microscopy and 3D profilometry (Fig. 3c–e and Fig. S14 and S15), yielding a healing efficiency of 99.7 ± 0.1%. Achieving complete scratch healing at room temperature addresses a key limitation of many reported self-healing conductors, which

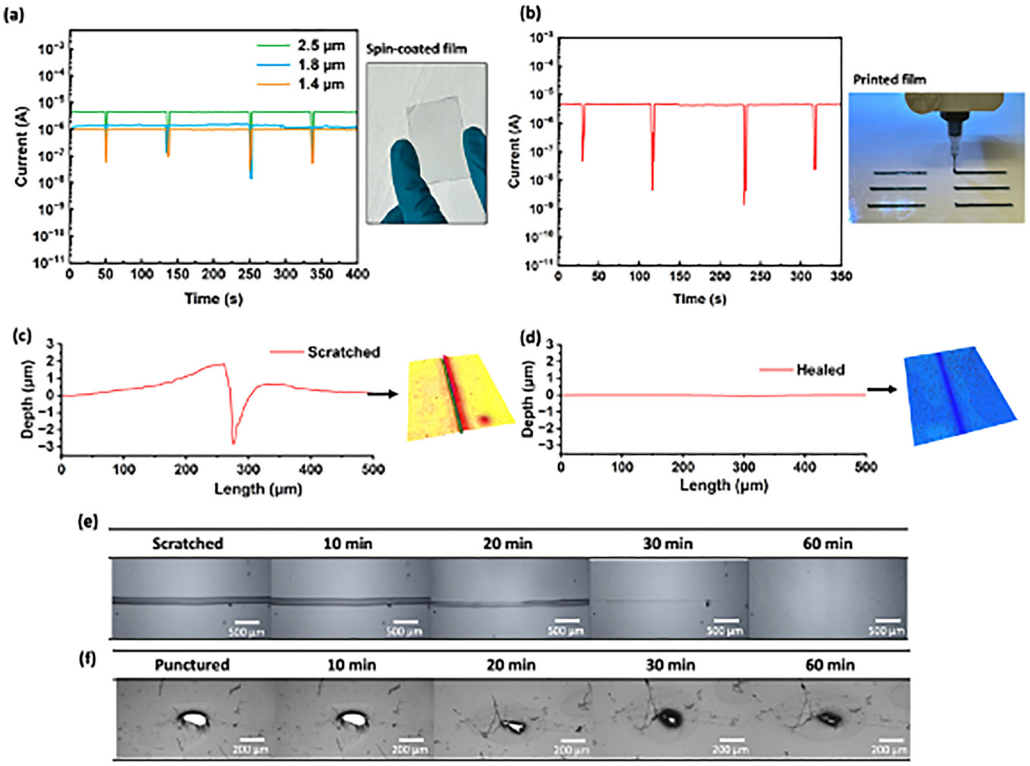

Fig. 3 Electrical and mechanical self-healing behavior of the optimized formulation. (a) Current–time response of spin-coated films with thicknesses of 2.5, 1.8, and 1.4 μm during repeated cut–healing cycles under a constant 0.2 V bias and photo of transparent film. (b) Current–time response of printed films during repeated cut-healing cycles and image of printed conductive traces fabricated on tattoo paper using direct ink writing. (c and d) Depth profiles and three-dimensional optical profilometry maps of the films (c) after surface scratching with a 3N pencil and (d) after healing at 25 °C. The color scale represents surface height variations, with red/yellow indicating deeper regions and blue corresponding to nearly flat surfaces. (e) Optical microscopy images of the film surface before and after healing of pencil-induced scratches. (f) Optical microscopy images showing puncture damage and subsequent recovery of the punctured region of a free-standing membrane after healing at room temperature. All experiments were performed in triplicate (n = 3).

typically require elevated temperatures or external stimuli to restore surface integrity.

Beyond scratches and cuts, our composites exhibited the rare and highly desirable ability to self-heal after puncture damage. Puncture-induced defects, which create localized disruptions, pose a severe challenge for solid-state systems and have been seldom explored in conductive polymers. Holes were introduced using a stainless-steel needle, and the recovery process was monitored by optical microscopy (Fig. S16a). The freestanding membranes exhibited near-complete restoration of the punctured area within 1 hour at room-temperature, with minimal residual traces (Fig. S16b), which mainly arise from slight reflectivity difference under optical microscopy (Fig. 3f).

Puncture healing is evaluated qualitatively, as local electrical measurements are not well correlated with puncture closure in continuous thin films. Similarly, global tensile measurements are not representative, as the puncture diameter is negligible relative to the overall sample dimensions.

Unlike previous puncture healing demonstrations in liquid metal–based composites,[37,38] these results demonstrate that a fully solid-state conducting polymer can autonomously recover from severe mechanical damage. Such solid-state puncture-healing capability is highly relevant for ensuring the long-term durability and reliability of flexible electronic systems, including e-tattoos and wearable health monitors, which are routinely exposed to accidental impact, puncture, and mechanical deformation during daily use.

Collectively, these results demonstrate the versatility of the optimized formulation, which rapidly restores both electrical conductivity and mechanical integrity at room temperature after damage. Notably, the ability of a fully solid-state conducting polymer to recover from puncture damage, a severe and rarely addressed failure mode, highlights its promise for reliable, long-term operation in flexible and stretchable electronic devices.

2.4.3. Proposed mechanism for self-healing. To gain deeper insight into the origin of the self-healing behavior, solid-state FTIR spectroscopy was employed to probe the reversible interactions most likely to govern damage repair in the PEDOT:PSS/PU system. In particular, the analysis focused on S–S, C═O, and N–H vibrational modes, as these correspond respectively to dynamic disulfide bonds and hydrogen-bonding motifs incorporated into the polyurethane backbone to enable autonomous network reconfiguration. Spectra were collected for pristine, scratched, and healed samples to directly monitor chemical changes within the damaged region, a step beyond

conventional comparisons between only pristine and healed films.

Across all samples, no significant peak shifts were observed for the S–S, C═O, or N–H vibrations, indicating that the chemical structure of the constituent polymers remained intact during damage and recovery. This observation confirms that self-healing proceeds through reversible interactions rather than permanent chemical transformations. The characteristic S–S stretching band at approximately 600 cm^{-1} decreased in intensity after scratching, indicating disruption of disulfide bonds within the polyurethane network (Fig. 4a). Upon healing at room-temperature, this band recovered nearly to its original intensity, consistent with reformation of S–S linkages. Similarly, the C═O stretching band at approximately 1720 cm^{-1} (Fig. 4b) and the N–H stretching band at approximately 3350 cm^{-1} (Fig. 4c) both weakened after damage and regained intensity following healing, consistent with reversible disruption and restoration of hydrogen-bonding interactions. Fig. 4d quantitatively summarizes these trends using normalized peak intensities referenced to the pristine state.

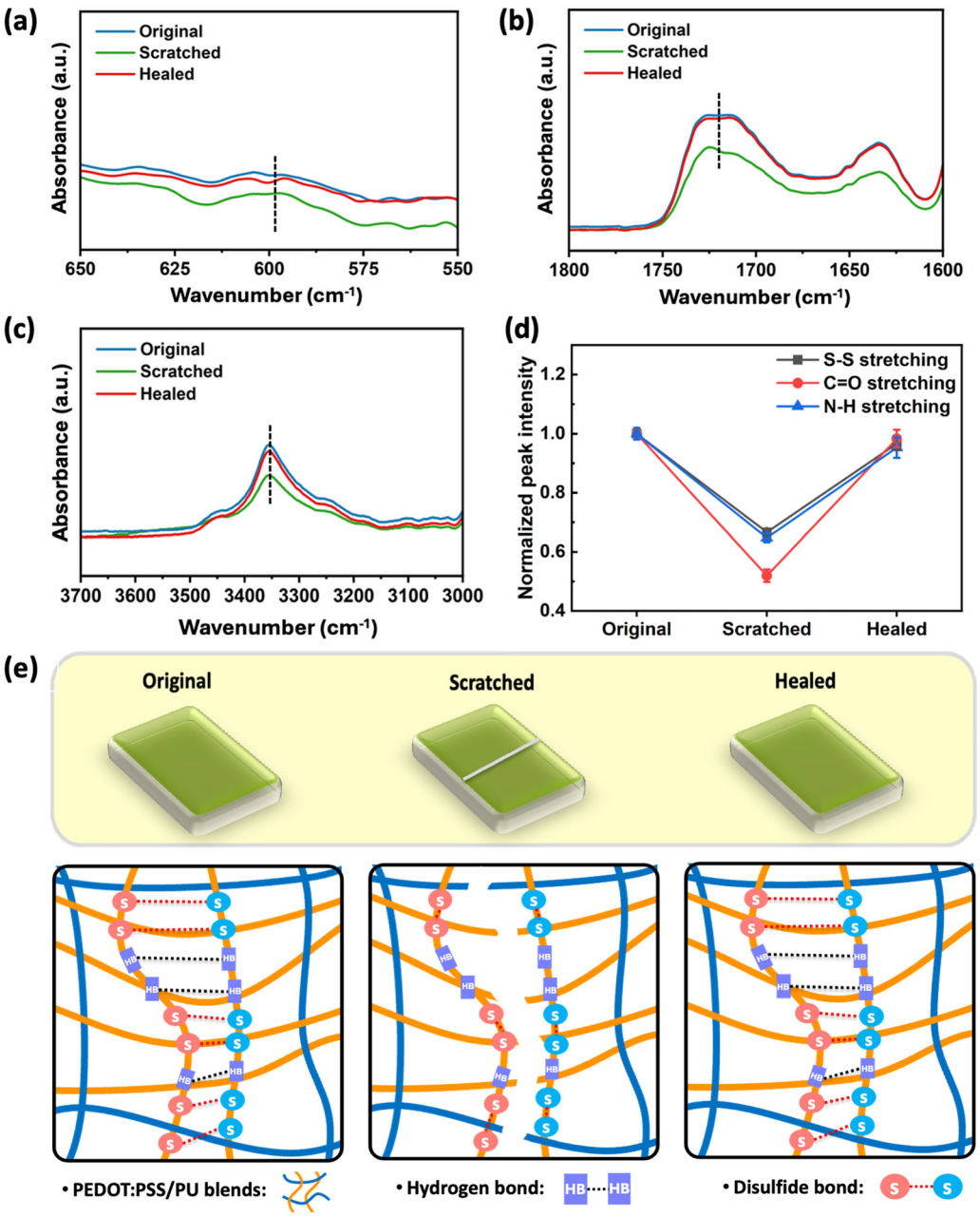

Fig. 4 FTIR analysis and proposed self-healing mechanism. (a–c) FTIR spectra acquired in the pristine, scratched, and healed states, highlighting regions corresponding to (a) S–S stretching, (b) C═O stretching, and (c) N–H stretching vibrations. (d) Normalized peak intensities referenced to the pristine state. All measurements were performed on three independent samples (n = 3). (e) Schematic illustration of reversible disulfide exchange and hydrogen-bonding interactions within the network in the pristine, damaged, and healed states.

Together, these observations support a self-healing mechanism driven by dynamic disulfide exchange and reversible hydrogen bonding (Fig. 4e), which enables polymer chain mobility and network reorganization at damaged sites without permanent chemical changes. Comparable spectral behavior observed for other PEDOT:PSS/PU formulations (Fig. S17) indicates that this mechanism is general across the material platform and underpins the robust room-temperature self-healing behavior of these composites.

To further substantiate the dynamic interactions, thermal and mechanical analyses were performed. DSC revealed a T_g of 21 °C (Fig. S10a), indicating sufficient chain mobility at room temperature. Consistently, stress relaxation measurements showed a gradual decrease in stress over time under constant strain (Fig. S18), with ~75% stress relaxation within 10 min, confirming efficient stress dissipation through dynamic network rearrangement. These results collectively support that reversible interactions not only exist but are actively involved in the self-healing process.

2.5. Demonstration of reliable ECG monitoring with printed PEDOT:PSS/PU-based E-tattoo electrodes

The mechanical compliance, printability, and damage tolerance of the optimized formulation enable its implementation as skin-conformal electrodes for flexible bioelectronics (Fig. 5a). Two device configurations were investigated: single-use tattoo electrodes and reusable freestanding electrodes. While tattoo electrodes are designed for one-time attachment using tattoo paper, printed freestanding films can be released, transferred onto skin, and subsequently removed with water for repeated reuse or recycling, as demonstrated in Fig. S19 and Movie S2. This dual-format capability highlights the versatility of the materials platform for wearable bioelectronics.

PEDOT-based tattoo electrodes have been widely investigated for skin-conformal electrophysiological monitoring due to their low interfacial impedance and improved wearer comfort compared with conventional Ag/AgCl electrodes.[39–42] Building on these advances, our electrodes introduce intrinsic self-healing, strong adhesion, and recycling–reuse capability without compromising electrical performance, representing an important step toward more durable and sustainable electronic tattoos for continuous health monitoring.[43,44]

Both electrode configurations enabled high-quality ECG recordings with stable waveform features comparable to those obtained using commercial Ag/AgCl gel electrodes (Fig. 5b), while exhibiting lower skin–electrode impedance across the measured frequency range (Fig. 5c). In both cases, the electrodes conform intimately to skin topography and maintain contact under compression, stretching, and twisting (Fig. S20). The films also displayed excellent water stability, with negligible swelling after 24 h immersion and only a minor reduction in elongation at break (Fig. S21). Importantly, freestanding electrodes retained clear ECG signals after multiple attachment–removal cycles (Fig. S22), underscoring their robustness and suitability for long-term wearable bioelectronic applications.

To quantitatively evaluate signal quality, the signal-to-noise ratio (SNR) was calculated for each electrode type (Fig. S23). The SNR values were 14.6 ± 0.3, 19.6 ± 0.5, and 19.9 ± 0.5 dB for the commercial, E-tattoo, and freestanding electrodes, respectively. The electrodes exhibited higher SNR compared

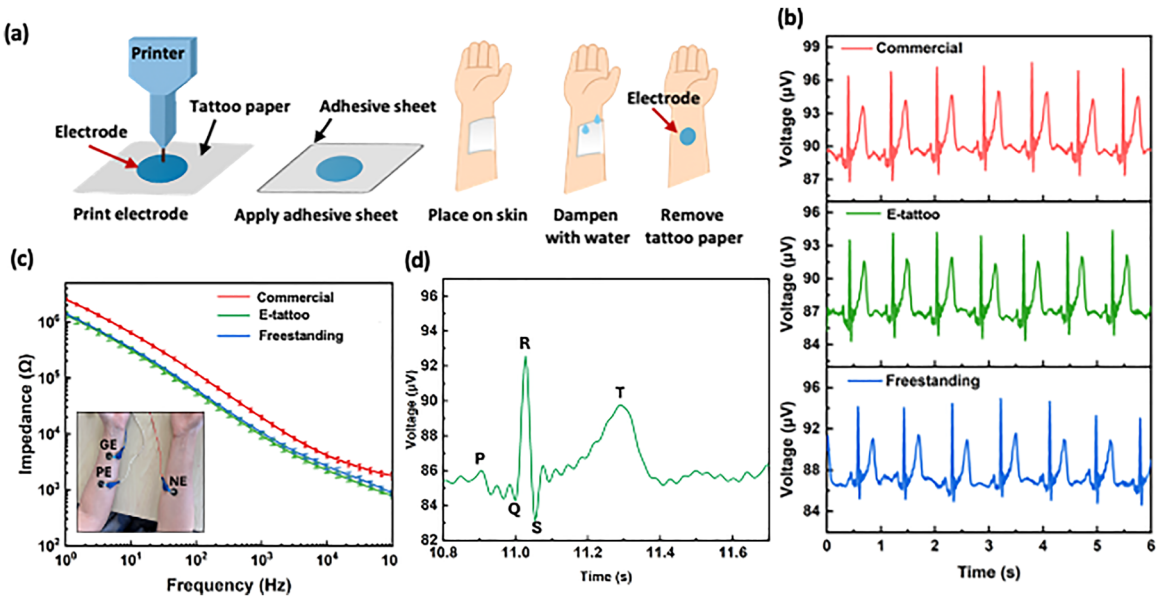

Fig. 5 (a) Schematic illustration of the fabrication process for printed electrodes on tattoo paper. (b) Representative electrocardiogram (ECG) recordings obtained using commercial Natus® Ag/AgCl gel electrodes, electronic tattoos (e-tattoos), and freestanding electrodes (n = 4 for each electrode type). (c) Comparison of skin–electrode impedance for commercial electrodes, e-tattoos, and freestanding electrodes (n = 4). Inset: photograph of the ECG measurement setup on a volunteer, showing the placement of the positive (PE) and ground (GE) electrodes on the left forearm and the negative (NE) electrode on the right forearm. (d) ECG signals recorded using E-tattoo electrodes. Well-defined P, Q, R, S, and T waves are clearly resolved, confirming stable and high-quality biosignal acquisition.

to the commercial Ag/AgCl electrodes, indicating improved signal clarity and reduced noise levels. These results confirm that the skin-conformal nature and stable interfacial contact of the printed electrodes contribute to reliable biosignal acquisition. Power spectral density (PSD) analysis (Fig. S24) revealed comparable spectral distributions across all electrode types within the ECG-relevant frequency range. The PEDOT:PSS/PU-based electrodes showed no increase in low-frequency drift (<1–2 Hz) or high-frequency noise (>30 Hz), and preserved signal characteristics in the main ECG band (~1–30 Hz), indicating that the improved SNR originates from enhanced interfacial stability rather than signal distortion. Furthermore, the recorded ECG signals exhibit clearly distinguishable P, Q, R, S, and T waves for both E-tattoo (Fig. 5d) and freestanding electrodes (Fig. Tensile stress–strain curves and (d) current–time responses of the original and recycled films, demonstrating recovery of mechanical and electrical performance after multiple recycling cycles (n = 3). In particular, the R-peaks are sharply defined and consistently detected, enabling reliable identification of cardiac cycles.

2.6. Chemical and mechanical recycling

Growing concerns over electronic waste highlight the need for sustainable recycling strategies that preserve the performance and value of soft electronic materials. To assess the circular potential of PEDOT:PSS/PU composites, both chemical recycling and mechanical reuse were investigated as complementary approaches enabling either component-level recovery or low-energy reshaping. Unlike most self-healing conductors that rely on permanent crosslinked networks or sacrificial additives,

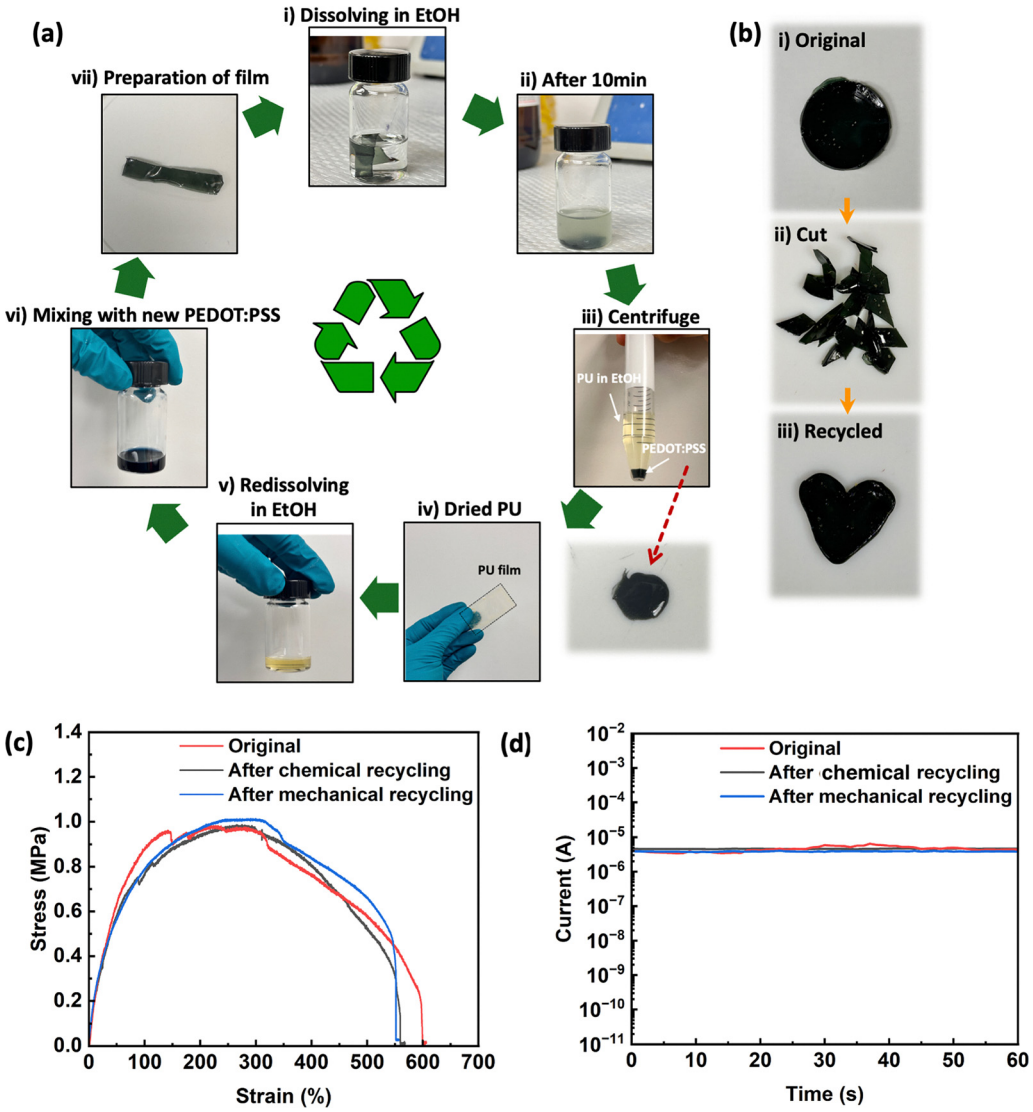

Fig. 6 Chemical and mechanical recycling of the composites. (a) Schematic illustration of the chemical recycling process (i–vii). (b) Mechanical reuse process, including cutting the composite into small fragments followed by remolding at 55 °C under light pressure to form continuous films (i–iii). (c) Tensile stress–strain curves and (d) current–time responses of the original and recycled films, demonstrating recovery of mechanical and electrical performance after multiple recycling cycles (n = 3). All electrical and mechanical data were collected over 15 recycling cycles, with three independently prepared samples measured per cycle (n = 3).

the present system supports both chemical recycling and mechanical remolding while retaining functional performance.

2.6.1. Chemical recycling. Fig. 6a was carried out by dissolving the composite in ethanol (EtOH), a green solvent compatible with both PEDOT:PSS and PU, enabling reprocessing without polymer degradation. This method allowed multiple recycling cycles while maintaining both mechanical and electrical properties. After a 10 min soak, centrifugation separated the PU-rich solution from the PEDOT:PSS phase. The PU fraction was readily redissolved, mixed with fresh PEDOT:PSS and glycerol, and re-cast into new composite films. Although the recovered PEDOT:PSS could not be fully redispersed, it still yielded conductive films upon drying (red arrow, Fig. 6a). This process was reproducible over multiple cycles, demonstrating an effective closed-loop recycling.

2.6.2. Mechanical reuse. Fig. 6b was evaluated by cutting the films into small fragments and remolding them at 55 °C under light pressure (Fig. 6b). The fragments rapidly fused into continuous films, confirming that dynamic disulfide and hydrogen bonds facilitate reprocessability.[45] After 15 recycling cycles, the films retained 95 ± 4% of their original elongation at break (Fig. 6c and Fig. S26a–c) and 98 ± 1% of their initial conductivity (Fig. 6d and Fig. S26d–f), confirming minimal degradation in performance. In addition, key mechanical parameters, including elongation at break, tensile strength, and Young's modulus, are summarized in Table S2 as a function of cycle number, enabling direct comparison of performance retention. Since thermal degradation occurs only above 280 °C (Fig. S10b), the mild 55 °C processing temperature prevents polymer degradation and represents a significantly energy reduction compared to the ~100 °C required in our previous system,[24] enhancing the overall sustainability of the process.

A comparison with reported self-healing conductors (Table S3) highlights that our composite integrates a combination of performance metrics that is rarely achieved simultaneously within a single conducting polymer system. In particular, the material combines autonomous room-temperature electrical self-healing with rapid recovery after cutting (≈0.1–0.3 s), effective healing of puncture damage on the hour timescale, large stretchability (~630%), and high healing efficiency (close to 100%) across multiple damage modes, including cuts, scratches, and punctures. Notably, autonomous electrical self-healing is achieved in continuous films as thin as 1.4 μm, whereas many previously reported self-healing conductors are primarily demonstrated in substantially thicker, drop-cast films, where electrical reconnection is less demanding. In addition, while recyclability is often limited or absent in many self-healing systems, the present composite supports both mechanical reuse and chemical recycling over multiple cycles with minimal loss of mechanical or electrical performance. Together, these attributes position the material among the highest-performing self-healing conducting polymer systems currently available, as many reported approaches focus on only specific aspects such as stretchability, conductivity, or single-mode healing.[46–51]

3. Conclusions

In this work, we developed a multifunctional PEDOT:PSS/PU composite that integrates room-temperature self-healing, recyclability, printability, and mechanical compliance within a single material platform. The rationally designed polyurethane matrix, incorporating dynamic disulfide bonds and hydrogen-bonding motifs, enables autonomous recovery from scratches, cuts, and punctures without external stimuli, while preserving high electrical conductivity, strong adhesion, and outstanding stretchability. The use of green solvents further supports the fabrication of uniform, transparent, and transferable films by spin-coating or printing, facilitating integration into flexible and stretchable electronic architectures.

Solid-state FTIR analysis confirms that the self-healing behavior arises from reversible intermolecular interactions—specifically disulfide bond exchange and hydrogen-bond reformation—rather than permanent chemical changes. These dynamic interactions allow the polymer network to reorganize efficiently and restore both structural and electrical continuity after damage.

Importantly, the composite supports both mechanical reuse and chemical recycling over multiple cycles with minimal loss of mechanical or electrical performance, underscoring its potential as a circular electronic material. Printed electronic-tattoo electrodes fabricated from this composite exhibit stable, low-impedance ECG recordings and enable facile detachment and reuse, validating their suitability for wearable bioelectronic applications.

Together, these results demonstrate that self-healing conductors can extend beyond surface damage repair to tolerate severe mechanical deformation while maintaining functionality. By uniting printability, autonomous room-temperature self-healing, and recyclability within a single PEDOT:PSS-based composite, this work provides a practical materials strategy for improving the durability, sustainability, and manufacturability of flexible electronic systems.

4. Experimental section

4.1. Materials

Clevios™ SV3 STAB, a screen-printing paste based on poly(3,4-ethylenedioxythiophene) doped with polystyrene sulfonate (PEDOT:PSS), containing diethylene glycol and propylene glycol, was purchased from Heraeus Precious Metals (Germany). Polycaprolactone diol (PCL diol, number average molecular weight of 2000 g mol^{-1}), polyethylene glycol (PEG, average molecular weight of 2000 g mol^{-1}), trimethylolpropane (TMP, >98%), dimethylformamide (DMF, >99.5%), anisole (>99%) and acetonitrile (>99%) were purchased from Millipore Sigma (St. Louis, MO, USA) and used as received. Isophorone diisocyanate (IPDI, >99%), aminophenyl disulfide (APDS, >98%), and dibutyltin dilaurate (DBTDL, >95%) were acquired from Tokyo Chemical Industry (USA). Ethanol (EtOH, >95%), Acetone (>95%), Isopropanol (IPA, >95%), purchased from Millipore Sigma, were used as received. Glass slides were obtained

from Corning (USA). A polytetrafluoroethylene (PTFE, Teflon™) mold was purchased from McMaster Carr. Polyethylene terephthalate (PET, XF-122, 25 μm thickness) sheets were purchased from Polyonics (USA). Tattoo paper was purchased from Sunnyscopa.

4.2. Synthesis of polyurethane (PU)

The synthesis of polyurethane (PU), illustrated in Fig. 1a, was carried out in ambient atmosphere in a three-necked round-bottom flask, which was purged with nitrogen for 15 min to remove oxygen and moisture prior to each reaction. PCL diol (3 g, 1.5 mmol), PEG (8 g, 4 mmol), IPDI (2.45 g, 11 mmol), and APDS (1.18 g, 5.5 mmol) were used in a molar ratio of 1.5 : 4 : 11 : 5.5, according to the stoichiometry. IPDI and the chain extender APDS formed the hard segments, PCL diol and PEG the soft segments and TMP acted as the crosslinker. PCL and PEG were dissolved in DMF (10 g) and heated at 80 °C under stirring. IPDI and the DBTDL catalyst (0.09 g) were then added dropwise. The reaction proceeded for 2.5 h to form an –NCO-terminated prepolymer. Separately, APDS and TMP (0.1 g, 0.5 mmol) were dissolved in DMF (10 g) and added to the prepolymer solution. The mixture was reacted for 2 h at 55 °C to. The product was cast into a Teflon mold and dried at 120 °C for 24 h to yield solid PU.

4.3. Preparation of PEDOT:PSS/PU composite films

The PEDOT:PSS paste was homogenized using a centrifugal mixer (ARM-310, Thinky, USA) at 2000 rpm for 5 min, then diluted with DMF (50 : 50 w/w). Solid PU was redissolved in DMF (30 wt%) and stirred until homogeneous using a vortex mixer (VWR). When required, glycerol was added as a plasticizer and conductivity enhancer. Final mixtures (compositions in Table 1) were obtained by blending PEDOT:PSS and PU solutions at the desired ratios and homogenizing with a vortex mixer.

Films were prepared by drop-casting onto glass slides (5.0 × 7.0 cm^2) and PTFE molds, spin-coating onto glass slides (2.0 × 2.0 cm^2) or PET substrates, and printing on glass slides and tattoo paper, as described in Section 2.9. Drop-cast films were sequentially baked on a hot plate at 50 °C for 16 h, 100 °C for 1 h, 120 °C for 1 h, and 150 °C for 1 h. Spin-coated films were deposited at 500, 1000, and 1500 rpm for 10 s, yielding thicknesses of 2.5, 1.8, and 1.4 μm, respectively, followed by baking at 50 °C for 3 h and 150 °C for 1 h. Both methods produced uniform, bubble-free films. Optical transmittance was evaluated by UV-vis spectroscopy (AS SEC2022, Bio-Logic). In addition to DMF, the films also dissolved in green solvents such as anisole and ethanol.

4.4. Thermal analysis

Thermogravimetric analysis (TGA, Q500, TA Instruments) was performed under N_2 (40 mL min^{-1}) from 30 °C to 800 °C at a heating rate of 10 °C min^{-1}. Films (~15 mg) were placed in open platinum crucibles. All samples exhibited onset decomposition near 300 °C, well above the temperatures required for healing (25 °C) and recycling (55 °C). No significant mass loss from DMF evaporation was observed, indicating minimal residual solvent.

Differential scanning calorimetry (DSC, Q2000, TA Instruments) was performed on ~5 mg films sealed in Al pans under N_2. To erase thermal history, samples were cooled to −25 °C, then heated to 150 °C at 10 °C min^{-1} twice. The T_g was determined from the second heating cycle, using a software provided by TA Instruments.

4.5. Attenuated total reflectance Fourier-transform infrared spectroscopy (ATR-FTIR)

Solid-state ART-FTIR spectra were collected using a Perkin-Elmer Spectrum 65 spectrometer (ATR mode, 4 cm^{-1} resolution, 32 scans, 4000–550 cm^{-1}). Measurements were performed before and after scratching and healing, focusing on the N–H, C═O, and S–S bonds to monitor dynamic bond reformation upon self-healing.

4.6. Electrical characterization

The sheet resistance (R_s) of 1 × 1 cm^2 films was measured using a four-point probe system (Jandel Engineering) connected to a Keysight B2902A source-measure unit (SMU). Resistivity (ρ) was calculated as $\rho = R_s \times t$, where R_s is the measured sheet resistance and t is the film thickness, obtained with a 3D optical profilometer (Photomap, Fogale Nanotech). Resistivity ($\rho = R_s \times t$) and conductivity ($\sigma = 1/\rho$) were averaged over five replicas.

Cyclic voltammetry (CV) measurements were using a VSP-300 potentiostat (Bio-Logic) controlled by EC-Lab software. A three-electrode configuration was employed, with the PEDOT:PSS/PU-18/Gly-2.2 film coated on an ITO substrate as the working electrode, an Ag/AgCl electrode as the reference electrode, and a platinum coil as the counter electrode. The measurements were carried out in a 0.1 M NaCl aqueous solution at a scan rate of 10 mV s^{-1} over a potential window of −0.9 to 0.9 V.

4.7. Mechanical and electromechanical tests

Tensile and adhesion tests were performed using a Mach-1 V500csst MA009 mechanical tester (Biomomentum Inc.). Stress–strain curves of films (5 × 1 cm^2) were obtained at a crosshead speed of 500 mm min^{-1}. Adhesion strength was measured by attaching free-standing films (6 × 1 cm^2, thickness ~25 μm) to themselves or to glass substrates and peeling them at 90°, in accordance with ASTM D6862, over a 3 cm length at 50 mm min^{-1}.

Cyclic tensile tests were performed for 700 cycles at 50% strain and 10 mm min^{-1}. Electromechanical stability was assessed using a custom-built uniaxial translational manipulator coupled to the Keysight B2902A. The film resistance was continuously monitored under cyclic loading at a constant bias of 0.2 V. Additional tests involved stretching the films to 400% strain at the same voltage and rate. Resistance changes were normalized as R/R_0, where R and R_0 denote the instantaneous and initial resistance, respectively.

Unless otherwise stated, all mechanical and electrical measurements were performed on three independently prepared

samples (n = 3). Representative curves are shown in the main text for clarity, while the corresponding replicate measurements are provided in the SI to demonstrate reproducibility.

Stress relaxation behavior was evaluated at room temperature (25 °C) using three independently prepared samples (n = 3). Films (5 × 1 cm^2) were stretched to a fixed strain of 50% at a constant strain rate and subsequently held at this strain while the stress decay was recorded as a function of time. The relaxation behavior was monitored for up to 10 min.

4.8. Electrical and mechanical self-healing

Electrical self-healing tests were performed in ambient atmosphere on drop-cast (1.0 × 5.0 cm^2, thickness of 2.5 μm) and spin-coated films with (thickness 1.8 μm, and 1.4 μm), using the Keysight B2902A SMU connected to two tungsten probes (miBots, Imina Technologies, Switzerland), placed at both ends of the film. A constant voltage of 0.2 V was applied while monitoring the current in real time. The films were manually cut several times at different locations using a razor blade (Feather Hi Stainless Double Edge, Japan) with a cut width of ∼20 μm, and the corresponding current variations were recorded to assess the self-healing performance. The cut-healing experiments were repeated at least three times. The electrical healing efficiency (η) was defined as the ratio of the recovered current after healing (I_{healed}) to the initial current before cutting (I_{original}), according to eqn (1)

$$\eta_{\text{electrical healing}}(\%) = 100 \times \frac{I_{\text{healed}}}{I_{\text{original}}} \quad (1)$$

Printed conductive traces (∼3 mm in width and ∼2 cm in length, thickness ∼15 μm) were fabricated on tattoo paper using the printing process as described in Section 4.9 and evaluated under the same electrical self-healing measurement conditions (0.2 V bias two prove configuration). The printed trace was cut using the same razor blade method, and the corresponding current changes during damage and healing were monitored.

Free-standing membranes (1.0 × 5.0 cm^2, thickness ∼25 μm) were used to investigate the mechanical self-healing, under scratching, cut-stick, and puncturing conditions. For the scratch test, a 3N load was applied using a scratch pen (Erichsen SmartPen, test tip ISO1518; diameter of 1.0 mm). The films were then kept at 25 °C for 1 hour on a hot plate to allow self-healing. The depth of the scratched regions before and after the healing process was measured using a 3D optical profilometer (Fogale Nanotech Photomap), and images were captured with the integrated optical microscope. Each test was repeated on three films. The mechanical healing efficiency for scratching (η) was calculated according to eqn (2):

$$\eta_{\text{scratch healing}}(\%) = 100 \times \frac{d_{\text{damaged}} - d_{\text{healed}}}{d_{\text{damaged}}} \quad (2)$$

where d_{damaged} is the depth of the scratch after damage and d_{healed} is the depth after healing.

For the cut-stick test, films (1.0 × 5.0 cm^2, thickness ∼25 μm) were cut into two pieces using a stainless-steel double-edge razor blade. The two pieces were then placed on a hot plate at 25 °C for 20 min, with their fractured edges in contact. A small amount of pressure was applied manually initially to maintain contact during healing. Tensile tests were performed before and after healing at a constant rate of 10 mm min^{-1}, using a 70 N load cell and mechanical tester. Three samples were tested. The mechanical healing efficiency for the cut-stick was defined as the ratio of the elongation at break after healing (E_{healed}) to the elongation at break of the pristine film (E_{pristine}), according to eqn (3)

$$\eta_{\text{cut-stick healing}}(\%) = 100 \times \frac{E_{\text{healed}}}{E_{\text{pristine}}} \quad (3)$$

For the puncture healing test, a needle with a 0.5 mm diameter (stainless steel sewing pin, China) was mounted to a mechanical tester (Biomomentum). The membrane (1.0 × 5.0 cm^2, thickness ∼25 μm) was placed onto a square rubber frame with an open center to allow the needle to fully penetrate the material (Fig. S27). The needle was driven downward and upward at a speed of 10 mm s^{-1} to puncture the films, generating a force of ∼3N. The punctured films were placed on a hot plate at 25 °C for 1 h to allow self-healing. Optical images were obtained using an inverted optical microscope (Carl Zeiss, Primovert). The experiment test was repeated three times. Here, puncture healing is defined as the autonomous closure of through-thickness damage accompanied by recovery of surface continuity, rather than complete restoration of the original microstructure.

4.9. Printed e-tattoos and freestanding electrodes for ECG signal monitoring

A printing ink was prepared by dissolving drop-cast PEDOT:PSS/PU-18/Gly-2.2 films in ethanol (EtOH). The resulting low-viscosity ink was used to print ∼17 mm-diameter disks onto tattoo paper and glass substrates using a direct ink writing printer (Voltera Nova) equipped with a stainless-steel dispensing nozzle (Nordson EFD, ∼150 μm diameter) mounted on a 3 cc syringe. Printing was carried out at a dispense pressure of 500 and a print speed of 2000 mm min^{-1}. Ethanol was selected as a green solvent because it effectively dissolves both the polyurethane and PEDOT:PSS components, outperforming anisole, acetonitrile, and isopropanol (Fig. S28). Although a larger solvent volume is required compared to *N*,*N*-dimethylformamide (DMF), ethanol is fully compatible with the printer's nozzle membrane, whereas DMF is not. Electrode patterns were designed in DipTrace software. Printed samples were dried at 60 °C for 2 h to remove residual solvent.

For tattoo electrodes, the disc electrodes were first printed on the tattoo paper substrate. Subsequently, a transparent adhesive film featuring a central 10 mm hole to ensure direct contact between the electrode and the skin was laminated over the printed layer to provide mechanical stability and facilitate transfer onto the skin. The tattoos were then applied with the printed side facing the skin: the backing paper was wetted with water for approximately 10 s and gently peeled off, leaving the electrode adhered to the skin. A commercial snap-button connector (Ambu®) was attached to the exposed surface of the

printed electrode and secured using Tegaderm™ tape to maintain a stable electrical connection.

Freestanding electrodes were fabricated by printing the ink onto glass substrates. A few drops of water were applied to the printed film for 5 s, to enable detachment from the glass. The released electrodes were then transferred directly onto the skin, and electrical connections were established following the same procedure as for the tattoo-based electrodes. This approach demonstrates the material's compatibility with multiple transfer strategies and enhances user comfort during electrode removal.

Electrocardiogram (ECG) signals were recorded with an OpenBCI Cyton biosensing board at a 250 Hz sampling rate with a 0.5–40 Hz band-pass filter and 60 Hz notch filter, using our printed electrodes and commercial Ag/AgCl gel electrodes for comparison. All data were collected from the same volunteer on the same day, following previously reported protocols.[24] Written consent was obtained from the participant. The protocol for human experiments was approved by the research ethics board of Polytechnique Montreal (certificate CER-2021-04-D), in accordance with the Tri-Council Policy Statement: Ethical Conduct for Research Involving Humans (TCPS).

The signal-to-noise ratio (SNR) was calculated from the recorded ECG signals to quantitatively assess signal quality. The SNR was defined as:

$$\mathrm{SNR(dB)} = 20\log_{10}\left(\frac{A_{\mathrm{R}}}{\sigma_{\mathrm{noise}}}\right)$$

where A_{R} is the average amplitude of the R-peaks and σ_{noise} is the standard deviation of the baseline noise. The baseline noise was estimated from signal segments between consecutive heartbeats. R-peaks were identified from the ECG waveform, and their amplitudes were measured relative to the local baseline. The reported SNR values represent the mean ± standard deviation obtained from independent measurements (n = 4). Power spectral density (PSD) analysis was performed using fast Fourier transform (FFT) with a Hanning window in Origin software. The resulting spectra were used to compare the frequency-dependent noise characteristics of different electrode types. The analysis was conducted based on ECG signals collected from four participants.

4.10. Reuse and recycling procedures

PEDOT:PSS/PU-18/Gly-2.2 films were subjected to chemical recycling and mechanical reuse to assess their potential for circular reprocessing.

4.10.1. Chemical recycling. Chemical recycling was carried out to recover and reprocess the individual polymeric components of the composite. PEDOT:PSS/PU films were first immersed in ethanol (10 mL) for 10 min, during which the polyurethane (PU) matrix was selectively dissolved. The resulting suspension was centrifuged at 1500 rpm for 15 min to separate the PU-rich supernatant from the PEDOT:PSS precipitate. The recovered PU solution was drop-cast onto glass substrates and dried at 50 °C for 1 h to remove the solvent, yielding solid PU. The isolated PU was subsequently redissolved in ethanol to form a 30 wt% solution. To regenerate the composite, this PU solution was mixed with fresh PEDOT:PSS diluted in ethanol (50 : 50 w/w). The resulting mixture was drop-cast onto glass substrates and dried stepwise at 50 °C for 1 h followed by 80 °C for 1 h to remove ethanol while minimizing bubble formation. The mechanical and electrical properties of the recycled films were then evaluated to assess performance retention after chemical recycling.

4.10.2. Mechanical reuse. Mechanical reuse was achieving by reshaping the composite without altering its chemical composition. Drop-cast films were first prepared in a PTFE circular mold following the procedure described in Section 2.3. After cooling to room-temperature, the films were cut into small fragments and transferred to a rectangular mold, where light pressure was applied to ensure intimate contact between the pieces. The mold was then heated at 55 °C for 30 min to promote healing and remolding, followed by cooling to ambient temperature for 5 min prior to demolding. The remolded samples were subsequently characterized to evaluate their mechanical and electrical properties.

Author contributions

F. C. supervised the research, contributed to discussions and manuscript editing. J. K. conducted the experiments, analyzed the results and drafted the manuscript. Both authors read and revised the manuscript.

Conflicts of interest

The authors declare no conflicts of interest.

Data availability

The data supporting this study are available in the Zenodo repository at https://doi.org/10.5281/zenodo.19609901. The dataset includes raw and processed data used to generate the figures in the main text and supplementary information (SI), as well as microscopy images associated with material characterization and device performance. The SI contains detailed experimental procedures, supplementary figures and tables, additional mechanical and electrical characterization data (including stress–strain behavior, cyclic deformation, adhesion measurements, and resistance under strain), quantitative self-healing analyses (cut, scratch, and puncture tests), optical microscopy and 3D profilometry data, recycling and mechanical reuse experiments over multiple cycles, and supporting videos illustrating self-healing and electrode transfer and reuse. See DOI: https://doi.org/10.1039/d6mh00177g.

Acknowledgements

The authors thank G. Petrossian, S. Khoomortezaei and C. Kim for fruitful discussions. This research was supported by the Natural Science and Engineering Research Council of Canada

(NSERC) through a NSERC Discovery Grant awarded to FC (RGPIN-2025-05607). JK acknowledges the Fonds de recherche du Quebec Nature et technologies (FRQNT) and the Trottier Energy Institute for PhD scholarships. The equipment and infrastructure used in this study were acquired and maintained by the Canada Foundation for Innovation. We would like to acknowledge CMC Microsystems, manager of the FABrIC project funded by the Government of Canada, for the provision of products and services that facilitated this research.

References

1 J. Xue, D. Liu, D. Li, T. Z. Hong, C. B. Li, Z. F. Zhu, Y. X. Sun, X. B. Gao, L. Guo, X. Shen, P. C. Ma and Q. B. Zheng, *Adv. Mater.*, 2025, **37**, 2414620.
2 Y. C. Ren, F. Zhang, Z. Yan and P. Y. Chen, *Device*, 2025, **3**, 100676.
3 H. B. Li, P. Tan, Y. F. Rao, S. Bhattacharya, Z. L. Wang, S. Kim, S. Gangopadhyay, H. Y. Shi, M. Jankovic, H. Huh, Z. J. Li, P. Maharjan, J. Wells, H. Jeong, Y. Y. Jia and N. S. Lu, *Chem. Rev.*, 2024, **124**, 3220–3283.
4 H. U. Chung, A. Y. Rwei, A. Hourlier-Fargette, S. Xu, K. Y. Lee, E. C. Dunne, Z. Q. Xie, C. R. Liu, A. Carlini, D. H. Kim, D. Ryu, E. Kulikova, J. Y. Cao, I. C. Odland, K. B. Fields, B. Hopkins, A. Banks, C. Ogle, D. Grande, J. B. Park, J. Kim, M. Irie, H. Jang, J. H. Lee, Y. Park, J. Kim, H. H. Jo, H. Hahm, R. Avila, Y. H. Xu, M. Namkoong, J. W. Kwak, E. Suen, M. A. Paulus, R. J. Kim, B. V. Parsons, K. A. Human, S. S. Kim, M. Patel, W. Reuther, H. S. Kim, S. H. Lee, J. D. Leedle, Y. J. Yun, S. Rigali, T. Son, I. W. Jung, H. Arafa, V. R. Soundararajan, A. Ollech, A. Shukla, A. Bradley, M. Schau, C. M. Rand, L. E. Marsillio, Z. L. Harris, Y. G. Huang, A. Hamvas, A. S. Paller, D. E. Weese-Mayer, J. Y. Lee and J. A. Rogers, *Nat. Med.*, 2020, **26**, 418–426.
5 L. H. Jia, Y. H. Li, A. B. Ren, T. Xiang and S. B. Zhou, *ACS Appl. Mater. Interfaces*, 2024, **16**, 32887–32905.
6 M. Qi, R. Q. Yang, Z. Wang, Y. T. Liu, Q. C. Zhang, B. He, K. W. Li, Q. Yang, L. Wei, C. F. Pan and M. X. Chen, *Adv. Funct. Mater.*, 2023, **33**, 2214479.
7 X. P. Hao, C. W. Zhang, X. N. Zhang, L. X. Hou, J. Hu, M. D. Dickey, Q. Zheng and Z. L. Wu, *Small*, 2022, **18**, 2201643.
8 W. B. Ying, G. Y. Wang, Z. Y. Kong, C. K. Yao, Y. B. Wang, H. Hu, F. L. Li, C. Chen, Y. Tian, J. W. Zhang, R. Y. Zhang and J. Zhu, *Adv. Funct. Mater.*, 2021, **31**, 2009869.
9 J. Jung, S. Lee, H. Kim, W. Lee, J. Chong, I. You and J. Kang, *Nat. Commun.*, 2024, **15**, 9763.
10 Y. F. Guo, S. Chen, L. J. Sun, L. Yang, L. Z. Zhang, J. M. Lou and Z. W. You, *Adv. Funct. Mater.*, 2021, **31**, 2009799.
11 R. A. Lehane, A. Gamero-Quijano, S. Malijauskaite, A. Holzinger, M. Conroy, F. Laffir, A. Kumar, U. Bangert, K. McGourty and M. D. Scanlon, *J. Am. Chem. Soc.*, 2022, **144**, 4853–4862.
12 R. Singh, J. Tharion, S. Murugan and A. Kumar, *ACS Appl. Mater. Interfaces*, 2017, **9**, 19427–19435.
13 X. L. Hu, M. Xia, M. H. Zhang, W. Yang, F. Z. Yang and Y. J. Luo, *Energy Mater. Front.*, 2024, **5**, 158–174.
14 L. Yang, L. J. Sun, H. F. Huang, W. F. Zhu, Y. H. Wang, Z. K. Wu, R. E. Neisiany, S. J. Gu and Z. W. You, *Adv. Sci.*, 2023, **10**, 2207527.
15 B. R. Li, S. R. Ge, S. Zhao, K. Y. Xing, A. P. Sokolov, P. F. Cao and T. Saito, *Mater. Horiz.*, 2023, **10**, 2868–2875.
16 S. Zhang and F. Cicoira, *Adv. Mater.*, 2017, **29**, 1703098.
17 Y. Li, X. Zhou, B. Sarkar, N. Gagnon-Lafrenais and F. Cicoira, *Adv. Mater.*, 2022, **34**, 2108932.
18 Y. Li, X. Li, S. Zhang, L. Liu, N. Hamad, S. R. Bobbara, D. Pasini and F. Cicoira, *Adv. Funct. Mater.*, 2020, **30**, 2002853.
19 P. Kateb, J. Fan, J. Kim, X. Zhou, G. A. Lodygensky and F. Cicoira, *Flex. Print. Electron.*, 2023, **8**, 045006.
20 X. Zhou, P. Kateb, J. X. Fan, J. Kim, G. A. Lodygensky, B. Amilhon, D. Pasini and F. Cicoira, *J. Mater. Chem. C*, 2024, **12**, 5708–5717.
21 J. Y. Oh, S. Kim, H. K. Baik and U. Jeong, *Adv. Mater.*, 2016, **28**, 4455–4461.
22 X. Zhou, A. Rajeev, A. Subramanian, Y. Li, N. Rossetti, G. Natale, G. A. Lodygensky and F. Cicoira, *Acta Biomater.*, 2022, **139**, 296–306.
23 F. Dong, X. Yang, L. Guo, Y. Wang, H. Shaghaleh, Z. Huang, X. Xu, S. Wang and H. Liu, *J. Mater. Chem. A*, 2022, **10**, 10139–10149.
24 J. Kim, J. X. Fan, G. Petrossian, X. Zhou, P. Kateb, N. Gagnon-Lafrenais and F. Cicoira, *Mater. Horiz.*, 2024, **11**, 3548–3560.
25 D. K. Chattopadhyay and D. C. Webster, *Progr. Polym. Sci.*, 2009, **34**, 1068–1133.
26 T. K. Chen, J. Y. Chui and T. S. Shieh, *Macromolecules*, 1997, **30**, 5068–5074.
27 H. Zhang, Y. Shang, N. Li, X. Hu, Z. Ye, X. Zhang, L. Qu, X. Song, Y. He and K. K. Fu, *Compos. B: Eng.*, 2025, 112500.
28 Y. Chen, Z. H. Tang, Y. J. Liu, S. W. Wu and B. C. Guo, *Macromolecules*, 2019, **52**, 3805–3812.
29 A. Ahmed, M. Z. Rahman, Y. Ou, S. Liu, B. Mobasher, S. Guo and D. Zhu, *Constr. Build. Mater.*, 2021, **294**, 123565.
30 S. M. Harle, *Structures*, 2024, **60**, 105881.
31 Q. Liu, Y. B. Liu, H. Zheng, C. M. Li, Y. Zhang and Q. Y. Zhang, *J. Polym. Sci.*, 2020, **58**, 1092–1104.
32 X. X. Jian, Y. W. Hu, W. L. Zhou and L. Q. Xiao, *Polym. Advan. Technol.*, 2018, **29**, 463–469.
33 H. He and J. Ouyang, *Acc. Mater. Res.*, 2020, **1**, 146–157.
34 S. Savagatrup, E. Chan, S. M. Renteria-Garcia, A. D. Printz, A. V. Zaretski, T. F. O'Connor, D. Rodriquez, E. Valle and D. J. Lipomi, *Adv. Funct. Mater.*, 2015, **25**, 427–436.
35 X. J. Du, L. Y. Yang and N. Liu, *Small Sci.*, 2023, 3.
36 M. C. Liu, J. Zhong, Z. J. Li, J. C. Rong, K. Yang, J. Y. Zhou, L. Shen, F. Gao, X. L. Huang and H. F. He, *Eur. Polym. J.*, 2020, 124.
37 R. Tutika, A. B. M. T. Haque and M. D. Bartlett, *Commun. Mater.*, 2021, 2.
38 E. J. Markvicka, M. D. Bartlett, X. N. Huang and C. Majidi, *Nat. Mater.*, 2018, **17**, 618–624.

39 M. Namkoong, H. Guo, M. S. Rahman, D. Wang, C. J. Pfeil, S. Hager and L. M. Tian, *npj Flex. Electron.*, 2022, **6**, 41.
40 Y. Y. Liang, A. Offenhaeusser, S. Ingebrandt and D. Mayer, *Adv. Healthcare Mater.*, 2021, **10**, 2100061.
41 L. M. Ferrari, U. Ismailov, J. M. Badier, F. Greco and E. Ismailova, *npj Flex. Electron.*, 2020, **4**, 4.
42 L. Zhang, K. S. Kumar, H. He, C. J. Y. Cai, X. He, H. X. Gao, S. Z. Yue, C. S. Li, R. C. S. Seet, H. L. Ren and J. Y. Ouyang, *Nat. Commun.*, 2020, **11**, 4683.
43 R. R. Zhao, X. R. Yan, H. J. Lin, Z. D. Zhao and S. S. Song, *Chem. Eng. J.*, 2025, **510**, 161645.
44 J. Li, D. Z. Mo, J. Y. Hu, S. C. Wang, J. Gong, Y. J. Huang, Z. Li, Z. Yuan and M. Z. Xu, *Microsyst. Nanoeng.*, 2025, **11**, 87.
45 Q. Zhang, Y. Deng, C.-Y. Shi, B. L. Feringa, H. Tian and D.-H. Qu, *Matter*, 2021, **4**, 1352–1364.
46 C. X. Zheng, Y. Y. Yue, L. Gan, X. W. Xu, C. T. Mei and J. Q. Han, *Nanomaterials*, 2019, **9**, 937.
47 D. H. Kim, Z. A. Akbar, Y. T. Malik, J. W. Jeon and S. Y. Jang, *Nat. Commun.*, 2023, **14**, 3246.
48 Y. Wang, B. S. Park, V. P. Vu and S. H. Lee, *Polym. Eng. Sci.*, 2025, **65**, 1854–1867.
49 J. C. Zou, Z. X. Yang, J. Y. Liang, Y. F. Xie, M. M. Fan and X. Zhang, *Polymer*, 2024, **315**, 127826.
50 H. Y. Mao, Y. Y. Zhang, L. X. Zhao, H. Li, H. L. Wu and L. Lin, *ACS Appl. Polym. Mater.*, 2024, **7**, 164–174.
51 K. M. Zhu, L. Yang, X. Zhou, X. Zhang, Y. Y. Hao, F. Li, W. Q. Lei, Q. Wang and G. S. Wang, *Chem. Eng. J.*, 2025, **510**, 161515.